Applied Catalysis A: General 528 (2016) 36–43

Contents lists available at ScienceDirect

Applied Catalysis A: General

journal homepage: www.elsevier.com/locate/apcata

Feature Article

Iron functionalization on graphene nanoflakes using thermal plasma for catalyst applications

U. Legrand *, J.-L. Meunier, D. Berk

Plasma Processing Laboratory (PPL), McGill University, Chemical Engineering, Montréal, Québec, Canada

ARTICLE INFO

Article history:
Received 15 June 2016
Received in revised form 7 September 2016
Accepted 25 September 2016
Available online 26 September 2016

Keywords:
Graphene nanoflakes
Thermal plasma
Iron
Non-noble metal catalyst

ABSTRACT

Graphene nanoflakes (GNFs), a stack of 5–20 layers of graphene sheets, are generated here using methane decomposition in a thermal plasma followed by homogeneous nucleation of the 2-dimensional structures in the gas stream. The GNFs are functionalized with nitrogen and iron to improve their electrocatalytic activity. The iron functionalization step is carried out as a post-processing step within the same thermal plasma reactor used to grow the nanoparticles. Two different iron precursors are tested in the reactor, iron powder and iron (II) acetate solution. The iron source carried by a nitrogen flow is injected in the argon plasma, and parameters such as the plasma power, pressure, and the exposure time during functionalization are optimized for enhanced catalyst activity. Structure and composition of the resulting catalysts are characterized, and their electrocatalytic performances in terms of onset potential, half wave potential and current density show an increase compared to the non-functionalized GNFs. This study proves the ability to entirely produce a pure and highly crystalline graphene-based non-noble metal catalyst using a thermal plasma single batch process with simple precursors such as methane and nitrogen gas, and an iron powder or iron acetate solution.

1. Introduction

Fuel cells, and more particularly alkaline fuel cells (AFCs) form promising energy conversion devices already found in diverse applications, such as transport and portable electronic devices [1]. Based on the oxidation of hydrogen with oxygen or other oxidizing agents, they present the advantage of releasing water vapour as a product without any pollutants. One key component in AFCs is the catalyst that enables the hydrogen oxidation, and more particularly the oxygen reduction to occur at the low temperature of the device, typically 80 °C. Platinum still outperforms any other catalyst material, the drawbacks being price and availability [2]. Generally the oxygen reduction reaction (ORR) is the limiting factor in AFCs, and requires most of the overall catalyst loading. Decreasing the price of the catalyst is thus one of the major issues that needs to be addressed to allow AFCs to reach larger markets. This can be achieved by reducing the amount of platinum used or by replacing the platinum with a cost effective non-noble metal catalyst (NNMC) [3–8], which is resistant to corrosion.

The present research on NNMCs is mainly based on the enhancement of the electrocatalytic activity of nitrogen functionalized carbon-based matrices by the addition of iron. Iron atoms can first form catalytic sites when linked by four to six atoms of nitrogen to the carbon support; such active sites were studied by Jasinski more specifically for the activity of iron and cobalt phthalocyanine towards the ORR [9], while Kramm et al. evaluated and proposed possible active configurations of the Fe/N/C sites [10]. Unfortunately, it is very difficult to identify with certainty the presence of such sites in catalysts material. Iron can also be found in the form of iron oxide nanoparticles, which also catalyses the ORR [11]. Whether atomically dispersed catalytic sites or iron oxide nanoparticles are the active elements in the catalysts, the carbon-based matrix has to be resistant to corrosion and electrically conductive. Graphene materials provide good conductivity as well as resistance to corrosion from their relatively small defect concentrations, and so form excellent structures to support nitrogen-iron based functionalities and/or iron oxide nanoparticles [12–14].

Highly crystalline graphene has been shown to be the best candidate for the ORR because of its resistance to both acidic and basic environments, and its high electrical conductivity [15]. A common method to produce graphene is by the reduction of graphene oxide obtained by the exfoliation of graphite, resulting in a graphene containing a large number of defects in its crystalline structure [16].

* Corresponding author.
E-mail address: ulrich.legrand@mail.mcgill.ca (U. Legrand).

http://dx.doi.org/10.1016/j.apcata.2016.09.015
0926-860X/

Preparation of the graphene structure as a catalyst support material using for example the method developed by Proietti et al. [17] also generates additional defects in the structure, defeating the purpose of getting a highly crystalline graphene.

The present work intends to introduce a new and original method for the synthesis of a complete non-noble metal catalyst using a high temperature thermal plasma reactor. Introduction of iron to nitrogen functionalized graphene nanoflakes (N-GNFs) for producing active ORR catalysts has been demonstrated by Pascone et al. using a wet-chemical method as a post-production step [18]. One objective of the present paper is to take advantage of the high reactivity of the plasma environment in the GNFs synthesis phase and produce a ready-made iron catalyst in a single batch process. The reactor is first used to grow the graphene structure through homogeneous nucleation from the gas phase, as proposed by Pristavita et al. [19,20] in the production of the GNFs. It has been shown that nitrogen can be added to GNFs within the thermal plasma system resulting in low (~2 at% using the GNF nucleation stage) and high (~25 at% using the downstream afterglow plasma) functionalization levels [21]. Up to 70% of the overall nitrogen was found to be attached through pyridinic or pyrrolic sites on graphene in a similar way to the phthalocyanine structure [21]. The GNFs maintained a good crystalline structure after the different functionalization steps with both low and high contents of nitrogen.

The present study mainly focusses on testing and optimizing a second *in situ* post-synthesis step, namely the addition of iron to the N-GNFs structures within the same plasma reactor. The optimal conditions used for GNFs growth and nitrogen functionalization steps are maintained as defined in previous work [20]. Two sources of iron are tested here following the growth and the nitrogen functionalization of GNFs, these being (a) iron powder and (b) iron (II) acetate solution, both using nitrogen as a carrier gas. Experimental tests are performed under different operating conditions within the reactor in order to achieve both nitrogen and iron functionalization on the GNFs (N/Fe-GNFs) within a single overall batch process made without opening the reactor. The resulting materials are then characterized for the structure of the graphitic material, the atomic composition of the sample surface, and the activity in the ORR.

2. Experimental methods

2.1. Catalyst generation

The generation of GNFs following Pristavita et al.'s procedure [20] uses methane as a carbon source that is decomposed within an argon thermal plasma. The argon thermal plasma is generated by an inductively coupled plasma (TP-ICP) torch, with a power of 20 kW delivered to the torch while the pressure within the reactor is 55.3 kPa. GNFs are formed as small nuclei through homogeneous nucleation. Modelling studies provide indications that GNFs essentially grow laterally in a sheet-like geometry within a very narrow nucleation and growth temperature window of 3700–4900 K in the plasma decay zone [22]. The nanoparticles are deposited on the walls and at the end plate downstream of the reactor, these deposits being further functionalized in the plasma recombination zone. The experimental reactor is axisymmetric with respect to the flow pattern, including the exit flow that extends radially from the downstream endplate. This provides a very good match with the modelled 2-D geometry, and an experimental flow pattern having a true stagnation point flow geometry with no recirculation loops throughout the reactor [22]. A small amount of nitrogen is added during the growth, leading to nitrogen content up to 2 at% on the surface of the GNFs.

As indicated above, iron is added in two different forms by switching off the methane gas feeding and introducing the iron source without opening the reactor. The main tested parameters during the functionalization step are the type of iron source (powder or iron acetate solution), the pressure within the reactor, the power delivered to the ICP torch, and the exposure time to the iron vapour.

The first iron source is a mixture of two iron powders fed to the reactor using a PFV100-VM-NO powder feeder from Tekna. A mixture is used because large iron particles with a size range between 10 and 300 μm are easy to feed continuously but difficult to vaporize while small iron particles between 1 and 10 μm are easy to vaporize but difficult to feed; mixing the powders takes advantage of both aspects, i.e. a continuous feeding and a good rate of vaporization. The optimized amount of small particles is 30 wt% (weight percent) of the total weight of iron powder injected within the reactor. A flow of 1 slpm of nitrogen has been chosen in order to carry the flow rate of 10 mg/min of iron particles from the powder feeder to the reactor and help the implementation of iron atoms on the GNFs surface. The iron particles are injected in the plasma zone, 9 cm downstream of the ICP torch nozzle using a side port on top of the reactor. This type of injection overcomes difficulties of particle transport within the injecting probe of the ICP torch.

The second source of iron is a ferrous acetate solution at a concentration of 1 mg/mL. The introduction of 10 mL of this solution is made using a 20 mL stainless steel syringe from Chemyx, using a Nexus 3000 pump, delivering the solution at a flow rate of 1 mL/min. The liquid is carried to the reactor using a flow rate of 1 slpm of nitrogen. In contrast to the iron particles, the ferrous acetate solution is fed through the injection probe of the ICP torch in the core of the plasma. It is expected that the difference in location of the iron source injection has a minor influence on the resulting vaporization, both streams being effectively injected within a relatively large volume having a temperature field range of 6500–7500 K occurring downstream of the torch nozzle [16]. In contrast, the physical state of the precursors in the form of a liquid solution or solid particles is dominant in controlling the quantity of iron vapour generated in the stream. Because of practical injection considerations generating different iron mass feeds, the amounts of iron vapour generated from the two sources are different. Also, it is expected that the level of iron functionalization is going to differ from one iron source to the other.

Two specific conditions for the power delivered to the ICP torch as well as the pressure within the reactor are chosen, namely 20 kW/55.3 kPa (8 psia) and 25 kW/13.8 kPa (2 psia). These were established through the theoretical modelling of the temperature and flow fields in the reactor showing that these two pairs of values presented similar temperature distribution profiles with the core of the plasma jet in the ICP torch reaching 10,000 K, and the walls of the reactor being cooled at 300 K [22]. The main difference between the two power/pressure conditions is in the velocity profiles. The maximum calculated velocity of the plasma, 160 m/s in the 13.8 kPa case, is four times greater than that in the 55.3 kPa case [23]. It is expected that the difference in the velocities and consequently in the residence time of the excited species in the plasma recombination zone would influence the iron functionalization of the GNFs. Also, the exposure time of the GNFs to the iron vapour is expected to be a key factor in the iron functionalization step. A short exposure time would lead to an insufficient amount of catalytic sites generated while a long exposure time could overload the samples with iron when considering the limited amount of the nitrogen-based host sites. The overall tested conditions are summarized in Table 1.

2.2. Physical characterization

The structure of the N/Fe-GNFs was studied using Scanning Electron Microscopy (SEM) on a FEI Inspect F-50 FE-SEM and Transmission Electron Microscopy (TEM) on a FEI Tecnai G2 F20 200 kV

Table 1
Experimental conditions of the iron functionalization step.

Iron Source	Power/pressure	Exposure time (min)	Sample name
Iron powder	20 kW/55.3 kPa	05	N/Fe-GNF1
		10	N/Fe-GNF2
	25 kW/13.8 kPa	05	N/Fe-GNF3
		10	N/Fe-GNF4
Iron Acetate	20 kW/55.3 kPa	05	N/Fe-GNF5
		10	N/Fe-GNF6
	25 kW/13.8 kPa	05	N/Fe-GNF7
		10	N/Fe-GNF8

Cryo-STEM. Raman spectroscopy was used to give information on the graphitization of the samples, and was performed on an inVia Reflex confocal micro-Raman (Renishaw) with a laser emitting at a wavelength of 514.5 nm. X-ray Photoelectron Spectroscopy (XPS) was employed to investigate the chemical structure of the surface of the catalysts, using a Scientific K-Alpha XPS system from Thermo Scientific with an aluminium x-ray source on analysed surfaces of 400 μm spot size.

2.3. Electrochemical characterization

The activity of the resulting catalyst is studied using Rotating Disk Electrode (RDE) electrochemical analysis. The samples are prepared on 5 mm glassy carbon tips by drying a small volume (20 μL) of a catalyst ink made of N/Fe-GNFs, water, ethanol and Nafion©, resulting in a loading of 0.1 mg/cm^2 of catalyst. The tests are performed in an alkaline medium made of a 0.1 M sodium hydroxide solution at room temperature, using a platinum wire counter electrode, and a saturated silver/silver chloride (Ag/AgCl) reference electrode. All tests are performed at a rotation speed of 2500 rpm. First, the catalysts go through a conditioning procedure consisting of repeated cycles between +1 and −1 V, at a scan rate of 500 mV/s, under N_2 bubbling in the medium. This procedure removes the impurities at the surface, allowing an optimal catalyst utilization [24]. After that, a background correction is done with linear sweeps between +1 and −1 V, at a scan rate of 20 mV/s, under N_2 bubbling. The background correction suppresses the contribution of capacitive current to the experimental ORR measurements [25]. Finally, the catalysts are tested when the medium is saturated by dissolved oxygen, through linear sweeps between +1 and −1 V, at a scan rate of 20 mV/s. The eight prepared samples are compared to the non-functionalized GNFs. The potential is converted from the Ag/AgCl reference to the reversible hydrogen electrode (RHE). Eq. (1) is used to convert the measured potential to RHE as follows:

$$E_{RHE} = E_{Ag/AgCl} + E^0_{Ag/AgCl} + 0.059pH \quad (1)$$

where $E^0_{Ag/AgCl}$ is the standard potential for Ag/AgCl electrode and equal to 0.1976 V. The pH of the sodium hydroxide solution has been measured at 13. The parameters used to compare the performances of the different candidates are the onset potential, the half-wave potential and the current density at 0.4 V.

3. Results and discussion

3.1. Structure of the N/Fe-GNFs

The structure of the catalysts was analysed by scanning and transmission electron microscopy (SEM, TEM). The SEM micrographs of two representative samples of both iron sources are shown in Fig. 1. The functionalized GNFs have a homogeneous and fluffy appearance, typical of this material [20]. It is important to note that the addition of carbon from the acetate ion is not seen to generate amorphous carbon, which would be recognizable by a cauliflower-like structure, or other impurities in the observed samples [26].

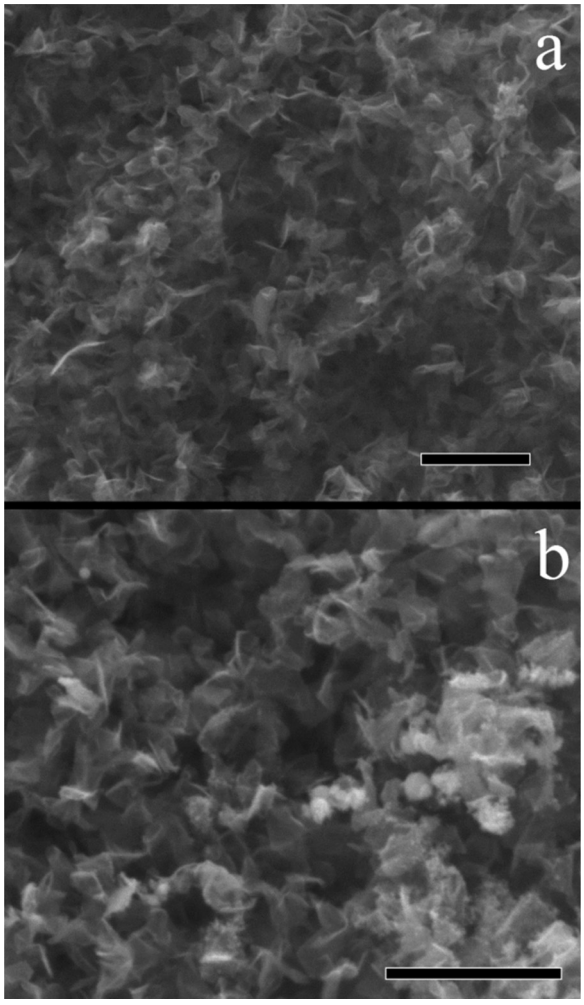

Fig. 1. SEM picture of the samples a) N/Fe-GNF8 and b) N/Fe-GNF1 for a scale bar of 500 nm.

Micro-particles of iron which have not completely evaporated have been found in the samples obtained with the iron powder source. As expected from the iron particle feed based on a 2-peak particle size distribution, the vaporization of iron particles is not complete. Spherical nanoparticles have been observed in samples from both iron sources, with the greater amount in the case of the iron powder source. In order to determine the nature of these nanoparticles, the samples have been analysed by TEM, and a micrograph from the sample N/Fe-GNF5 is shown in Fig. 2. Graphene nanoflakes are observed, and some of them appear to be covered by spherical nanoparticles. The size distribution of the spherical nanoparticles for the samples functionalized with iron acetate solution is 6.5 ± 2.2 nm, and 7.8 ± 2.6 nm when the iron source is iron powder. However, larger nanoparticles, up to 20 nm, have been observed with the iron powder source, such as the one depicted on Fig. 2. It can be seen that the repartition of the nanoparticles is not uniform. Some regions contain a large amount of spherical nanoparticles, while others do not contain any nanoparticles on the GNFs.

An energy dispersive X-ray (EDX) spectroscopy has been performed on the area containing the GNFs covered by the spherical nanoparticles, and compared to an area without presence of these nanoparticles. The EDX spectra reveal the presence of carbon, oxygen, iron, copper, and silicon. Carbon is the main component of the

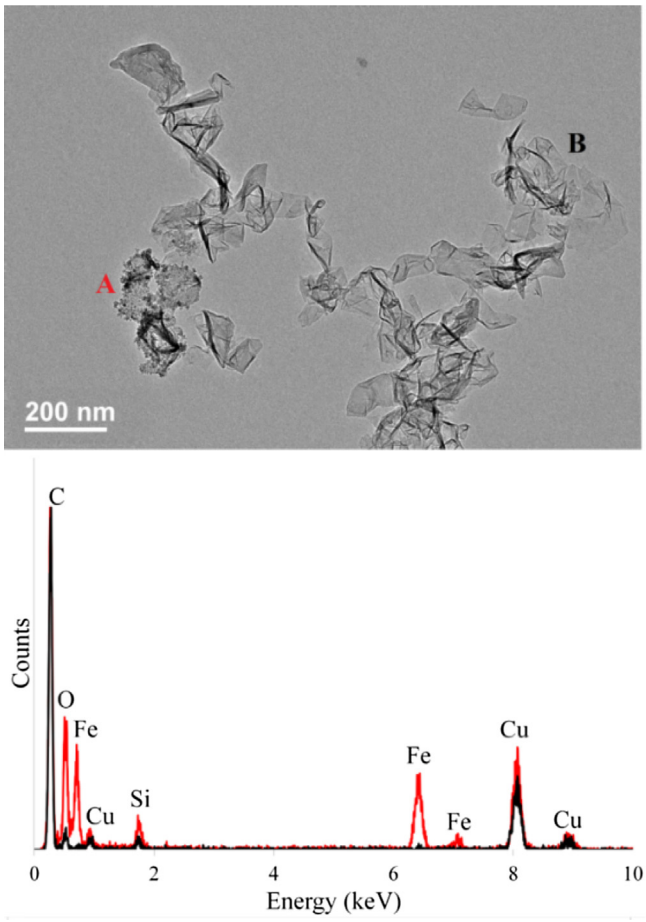

Fig. 2. TEM picture of N/Fe-GNF5 with a scale bar of 200 nm, with EDX spectra of the zone A, containing iron oxide nanoparticles (in red) and the zone B, containing only GNFs (in black). (For interpretation of the references to colour in this figure legend, the reader is referred to the web version of this article.)

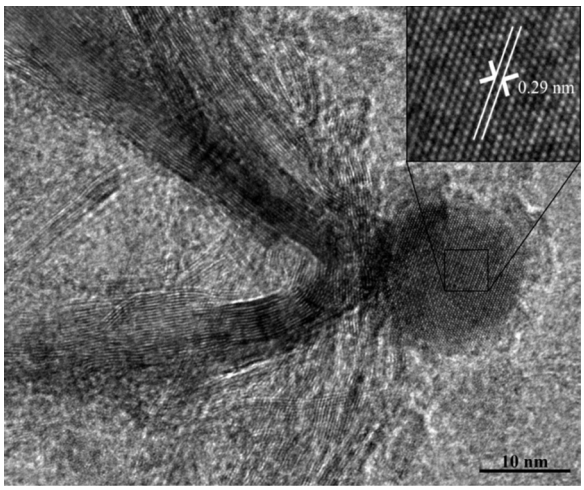

Fig. 3. High resolution TEM picture of N/Fe-GNF1.

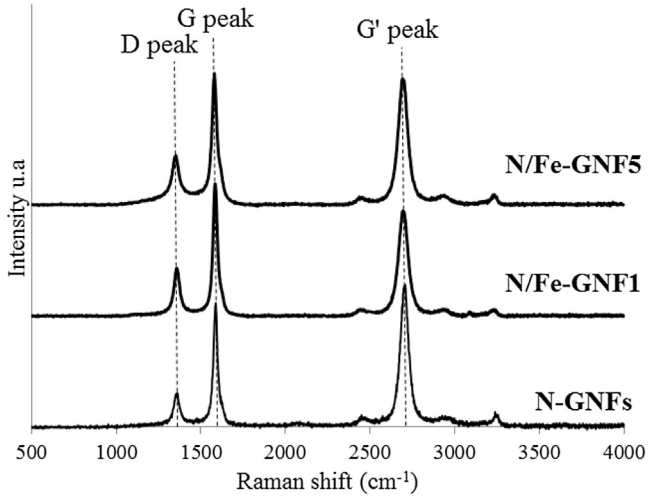

Fig. 4. Raman spectra for non-functionalized and two functionalized samples (N/Fe-GNF1 and N/Fe-GNF5).

GNFs, and the carbon peak was used to normalize both spectra. The presence of copper is explained by the copper grid used to deposit the samples while the trace amounts of silicon are impurities originating from the silicon grease used to seal the plasma reactor. By comparing the two spectra, it can be deduced that the spherical nanoparticles are made of iron oxide. Indeed, a small amount of oxygen is naturally present in the GNFs, but this amount drastically increases in the spherical nanoparticles area. The nature of the iron oxide has been determined by taking a closer look on the nanoparticles with the help of the high resolution TEM (HR-TEM) as seen on Fig. 3. The measurement of the interspacing distances between paralleled planes gives a distance of 0.29 nm, identified as the (220) interspacing distance for γ-Fe_2O_3 [27]. The interspacing distance has also been measured on other samples, and the interspacing distances of the planes (220), as well as the planes (100) have been found. The nature of the iron oxide is later confirmed by the XPS analysis.

The effect of the functionalization on the samples graphitization was analysed by Raman spectroscopy. Raman spectra of functionalized and non-functionalized samples are shown in Fig. 4, and exhibit several peaks of interest, typical of graphitic materials. The D peak, located at 1350 cm^{-1}, is correlated with the amount of non-graphitized carbon in the graphitic structure, while the G peak, found at 1580 cm^{-1}, is associated with the graphitized carbon contained in the sample. The G' peak at 2700 cm^{-1} sees its intensity and sharpness increased when the number of graphene sheets in the stack decreases. The quality of the graphitic material can be quantified by graphitic indices, such as the purity, the crystallite size (L_a) and the average length of graphene planes (L_{eq}), whose relations have been established by Larouche et al. [28], and are based on the intensity and underlying area of the D, G, and G' peaks. The crystallite size, L_a, represents the size of a defect-free area in the graphitic structure, while the average length of graphene planes can be represented by the total length of planar structures linked by curvature. The values of the graphitic indices for the functionalized and non-functionalized sampled are summarized in Table 2.

Table 2
Graphitic indices relations [28] and corresponding values for the GNFs samples.

Sample Relations	Purity (±0.2) I_G/I_D	L_a (±0.3 nm) $4.4 \times A_G/A_D$	L_{eq} (±0.5 nm) $8.8 \times A_{G'}/A_D$
N-GNFs	2.8	8.8	28.2
N-Fe/GNF1	2.8	9.2	26.6
N-Fe/GNF2	3.0	10.8	32.5
N-Fe/GNF3	2.6	8.8	30.2
N-Fe/GNF4	2.3	9.2	28.4
N-Fe/GNF5	2.7	8.6	26.2
N-Fe/GNF6	2.6	9.0	29.0
N-Fe/GNF7	2.6	8.9	24.4
N-Fe/GNF8	2.6	7.1	24.0

The values of the purity, as well as L_a and L_{eq} stay in the same range before and after functionalization, showing that the

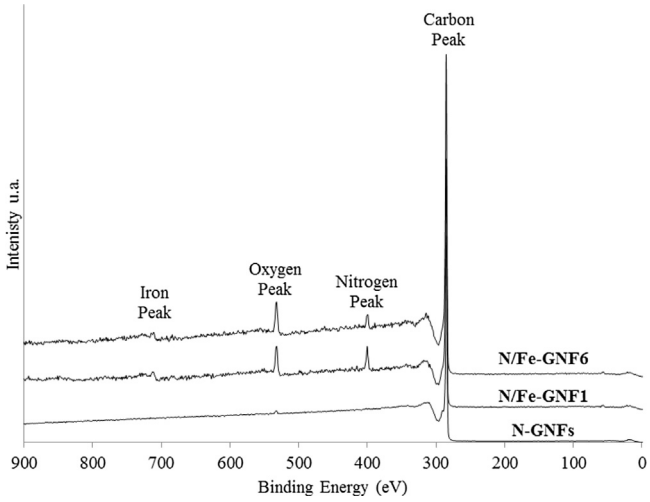

Fig. 5. XPS survey scan of two samples (N/Fe-GNF1 and N/Fe-GNF6) compared to the N-GNFs.

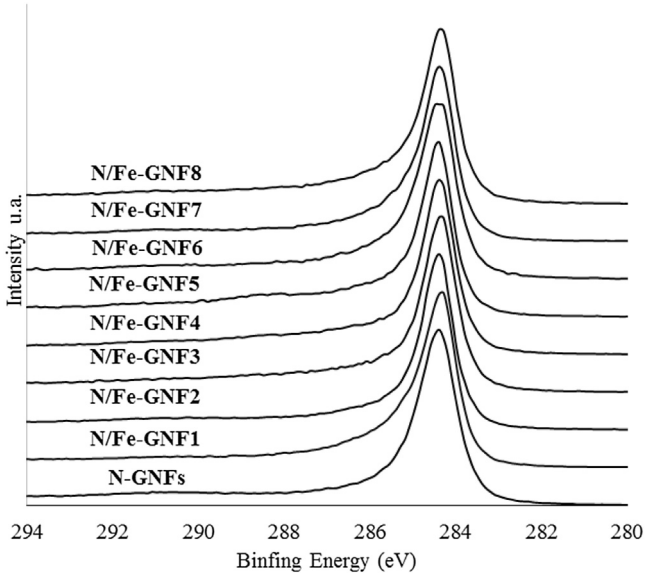

Fig. 6. High resolution of carbon C1s peak for the eight samples compared to the non-functionalized GNFs.

Table 3
Atomic composition at the surface of the N/Fe-GNFs.

Sample	C (at%)	N (at%)	O (at%)	Fe (at%)
N-GNFs	98.07	0.56	1.37	–
N-Fe/GNF1	91.53	4.76	3.54	0.18
N-Fe/GNF2	93.49	1.09	4.94	0.48
N-Fe/GNF3	89.39	4.50	6.01	0.10
N-Fe/GNF4	86.49	5.69	7.75	0.08
N-Fe/GNF5	89.31	4.79	5.79	0.11
N-Fe/GNF6	92.36	3.55	3.94	0.15
N-Fe/GNF7	89.25	4.60	6.09	0.06
N-Fe/GNF8	81.93	8.47	9.52	0.07

iron/nitrogen functionalization step seems to not deteriorate the graphitic structure of the GNFs by addition of defects. The purity, defined as the ratio of the G to D peak is generally close or lower than 1 for materials such as graphene oxide and reduced graphene oxide, widely used in the preparation of non-noble metal catalysts [16]. The GNFs exhibit values between 2.3 and 3, denoting a large amount of graphitized carbon and showing the higher crystallinity of the samples produced here.

3.2. Chemical composition of the N/Fe-GNFs

XPS was used to determine the atomic composition of the N/Fe-GNFs surface. The surveys of two representative samples from both iron sources compared to the survey of N-GNFs are shown in Fig. 5 while the composition of every single sample is given in Table 3 .

From the atomic composition given in Table 3 the functionalization step improves drastically the level of nitrogen and oxygen present on the surface of the GNFs. On average, the level of attached oxygen is greater for the iron source being iron (II) acetate solution (N/Fe-GNF5,6,7,8). This can be explained by the large amount of oxygen contained in water and acetate ions, compared to the oxygen contained in the iron powder in the form of a surface oxide layer. Also, the levels of nitrogen and oxygen are greater when the functionalization step takes place at high-power/low-pressure values of 25 kW/13.8 kPa (N/Fe-GNF3,4,7,8). Previous studies on the addition of nitrogen and oxygen have already shown that the low pressure and high power conditions resulted in higher incorporated amount of each element, these conditions causing much shorter transit times of the active species between the plasma and the GNF powders [21,23].

The exposure time during the functionalization step does not seem to correlate with the increasing level of oxygen or nitrogen in the GNFs. Indeed, the samples (N/Fe-GNF2,6) exposed to a functionalization step at 20 kW/55 kPa globally see their nitrogen and oxygen level decreasing when the exposure time is higher while the samples (N/Fe-GNF4,8) functionalized with a higher power and lower pressure have greater amounts of nitrogen and oxygen after a longer exposure time. The temperature fields being similar in both conditions, one may speculate that the higher thermal load expected in the low-power/high pressure condition may influence the loss of some nitrogen and oxygen functional groups on the N/Fe-GNFs structures.

The present results show the effect of the iron source on the iron functionalization. It appears that the iron powder source leads to more iron on the surface sample than the iron (II) acetate source. This difference may come from the different mass flow rates of iron between the two sources, ten times higher in the case of the iron powder. The amount of iron on the GNFs is also greater when the plasma conditions of the functionalization step are 20 kW/55 kPa, especially when the source is iron powder. This can be explained by the longer residence time of the powder in the hot regions of the plasma resulting in higher vaporization rates. The results on the amount of iron in the samples need however to be taken with precaution due to differences between the surface composition and the actual amount contained in the sample. For the iron powder as a source, 50 wt% of iron is actually present in the samples while the XPS results give values up to 0.48 at%, which would be equivalent to 2 wt% when considering the surface composition of the sample. The way iron oxide nanoparticles form and are deposited non-homogeneously on the GNFs as well as the presence of unevaporated micro-particles in the case of the iron powder source induce the differences in the reading of the level of iron at the surface and the actual amount of iron.

The high resolution XPS peaks of carbon for each sample are depicted in Fig. 6. The shape of the carbon peak, typical of a graphitic carbon, is similar before and after functionalization. Small differences can be detected in the region 285–289 eV, related to carbon-oxygen bonding. Indeed, the functional groups C—O, C=O and O—C=O are respectively associated with 285.5, 287.7 and 286.7 eV. The preservation of the carbon peak shape before and after functionalization indicates that most of the carbon from the samples remains in the sp^2 state, meaning that there is no trans-

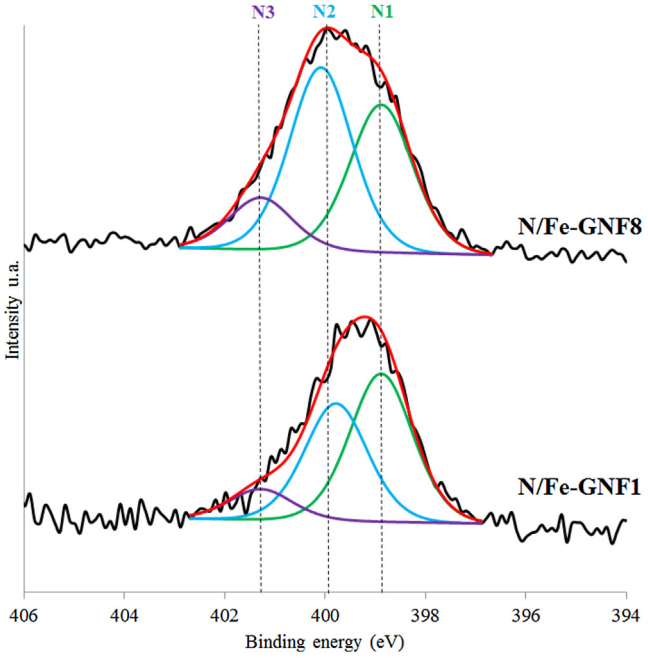

Fig. 7. High resolution and deconvolution peak of nitrogen N1s from the samples N/Fe-GNF1 and N/Fe-GNF8. N1, N2 and N3 are respectively associated to pyridinic, pyrrolic and graphitic nitrogen.

Table 4
Repartition of pyridinic (N1), pyrrolic (N2) and graphitic (N3) nitrogen species for each N/Fe-GNFs sample.

Sample	N1 (%)	N2 (%)	N3 (%)
N-Fe/GNF1	50.0	39.8	10.2
N-Fe/GNF2	34.3	38.3	27.4
N-Fe/GNF3	36.6	52.8	10.6
N-Fe/GNF4	38.2	50.9	10.9
N-Fe/GNF5	42.2	52.6	5.2
N-Fe/GNF6	38.0	51.4	10.6
N-Fe/GNF7	36.6	46.6	16.8
N-Fe/GNF8	38.6	47.9	13.5

formation of graphitic carbon into amorphous carbon, confirming the observation of the Raman spectroscopy.

The high resolution peaks of nitrogen for typical samples are represented in Fig. 7. The peaks are deconvoluted based on elementary Gaussian-Lorentzian fitting. The main binding energies used for the deconvolution are 398.9, 399.8 and 401.3 eV, respectively associated with pyridinic, pyrrolic, and graphitic nitrogen species. The ratios of the different type of nitrogen species for each functionalized samples are summarized in Table 4. No clear trend can correlate the experimental conditions to the resulting nitrogen species in the samples. The importance of each type of nitrogen for the ORR is still controversial in the literature, contradictory studies claiming pyridinic, pyrrolic or graphitic nitrogen is the specie responsible of the improvement of the electrocatalytic activity of the functionalized graphene sample [29].

When the iron peak is intense enough to be clearly identified, for example with sample N/Fe-GNF2, the state of the iron can be analysed (Fig. 8). The position of the 2p1/2 and 2p3/2 peaks, at 725 and 711 eV respectively, as well as their satellite position, located 8 eV higher than the main peaks, indicate that iron is in the oxidation state +III [30]. The absence of iron in the oxidation state +II confirms the nature of the iron oxide nanoparticles being Fe_2O_3. XPS analysis does not allow to discriminate iron atoms contained in iron oxide nanoparticles and iron surrounded by nitrogen atoms forming a

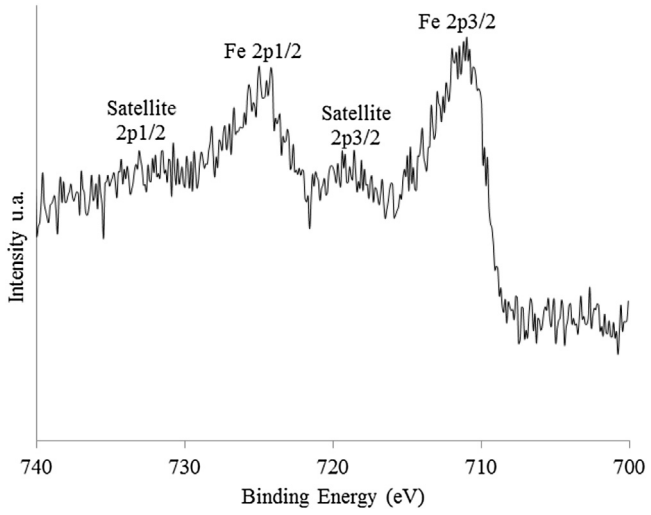

Fig. 8. High resolution of iron XPS peak from the sample N/Fe-GNF2.

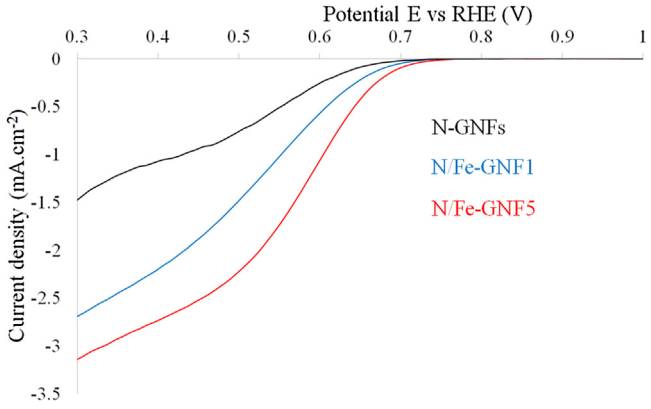

Fig. 9. Linear sweep voltammetry of samples N/Fe-GNF1 (blue) and N/Fe-GNF5 (red) compared to the N-GNFs in O_2 saturated 0.1 M NaOH, at a scan rate of 20 mV/s, for a rotation speed of 2500 rpm. (For interpretation of the references to colour in this figure legend, the reader is referred to the web version of this article.)

catalytic site [31]. However, iron oxide nanoparticles are expected to participate in the electrocatalytic activity of the materials.

3.3. Activity of the catalysts

The activity of the catalysts is tested by RDE. The performances of all of the catalysts are listed in the Table 5, based on the onset potential, the half wave potential and the current density, at −0.4 V [32]. The onset potential is defined where the electrocatalytic current can be distinguished from 0. The onset potential of platinum based catalysts is around 0.8 V vs RHE, a value where catalysts are considered to have good performances [32]. The half-wave potential is the reported potential where the intensity of the current density is reaching half of its maximum, and represents how sharp the increase of the current density is. The sharpness of the curves is directly related to the kinetics of the reactions; the sharper the curve is, the fastest the reaction is. The current densities, calculated based on the geometric surface area of the RDE electrode, have negative values due to the cathodic nature of the reduction reaction, and are proportional to the rate of reduction of oxygen. Overall, the lowest values for the current density are related to the best catalytic performances. Taking into account all these parameters, the results for the best samples respectively to both iron sources (N/Fe-GNF1 and N/Fe-GNF5) have been determined, and compared to the non-functionalized GNFs on Fig. 9. It can be argued that the

Table 5
Performance of the catalysts compared to the non-functionalized GNFs.

Sample	Onset Potential (V vs RHE)	Half-wave Potential (V vs RHE)	Current Density @ 0.4 V vs RHE (mA/cm^2)
N-GNFs	0.67	0.55	−1.06
N-Fe/GNF1	0.70	0.56	−2.16
N-Fe/GNF2	0.69	0.55	−1.87
N-Fe/GNF3	0.68	0.55	−1.38
N-Fe/GNF4	0.67	0.56	−1.06
N-Fe/GNF5	0.72	0.58	−2.71
N-Fe/GNF6	0.71	0.58	−2.21
N-Fe/GNF7	0.67	0.55	−1.11
N-Fe/GNF8	0.70	0.54	−1.65

onset potential for the iron-based samples produced in this method is lower than the one for the platinum-based catalysts. However, the overall catalytic performances are improved after the plasma functionalization step.

3.4. Discussion

The catalytic performances as measured by RDE are in a close range; however the differences observed between the catalysts enables some analysis on the influence of the plasma conditions generating these catalysts. Generally it appears that the catalysts having iron (II) acetate perform better than those having iron powder as a source.

In the case of the catalyst having iron powder as a source, the best plasma conditions for the functionalization step are 20 kW/55.3 kPa, for an exposure time of 5 min, corresponding to the sample N/Fe-GNF1. The catalysts which were treated with the 20 kW/55.3 kPa conditions perform better than those treated by plasma conditions with a higher power and lower pressure. As mentioned previously, the 20 kW/55.3 kPa conditions allow a longer residence time of the injected iron particles in the hot zone of the thermal plasma, increasing their evaporation rate and generating in this way more iron vapour leading to higher iron content in the samples. However, a too long exposure time of the GNFs to the iron powder leads to lower electrocatalytic performances. It is recognized that an excessive amount of iron in the catalyst has tendency to decrease the activity, which could lead to the overall lower performances for this iron source [7].

In the case of iron (II) acetate solution, a similar behaviour seems to affect the activity of the catalyst, where the optimal couple of power and pressure for the functionalization step is 20 kW/55.3 kPa, with a time of exposure of 5 min. The presence of water injected to the plasma requires energy to be vaporized and eventually decomposed. A higher residence time for the iron acetate solution in the hot region of the reactor could lead to a higher generation of iron vapour, leading to a better functionalization rate of the samples, as shown in the XPS analysis.

Most of the catalysts synthesized based on the plasma functionalization step show an improvement of their electrocatalytic activity when compared to the non-functionalized sample. The origin of this improvement is still controversial in the literature. No clear evidence has been found in this study to highlight the presence of catalytic sites for the ORR based on atomic iron surrounded by nitrogen atoms as is the case for the heme-B structure of blood and phthalocyanine. Iron oxide nanoparticles have however been detected in the samples. Studies have been conducted proving that iron oxide nanoparticles are improving the electrocatalytic activity of non-precious metal catalysts [11,33], and often mislead on the comprehension of the involved phenomena. The growth of iron oxide nanoparticles is a competitive process in the presented method due to the fact that the deposited GNFs are localized in cold areas of the thermal plasma reactor, where the temperature is below the melting temperature of iron (1811 K), allowing the diluted iron vapour to condense into iron oxide nanoparticles before being deposited on the surface of the GNFs [34]. The production of iron oxide nanoparticles can also be found in other functionalization methods, such as wet chemistry, due to the precipitation of iron in solution, which is a common method to produce this type of nanoparticles [27].

4. Conclusion

Non-noble metal catalysts for the oxygen reduction reaction have been completely produced by an original method where the carbon matrix is grown and the iron functionalization step is performed in the same thermal plasma reactor by changing the feeding gas conditions. An improvement of the electrocatalytic activity has been noticed for different conditions, depending on the iron source employed. Even if the performances of the catalysts are lower than platinum based catalysts, this study represents the proof of concept on the generation of non-noble metal catalysts from nucleation to various functionalization steps within a thermal plasma reactor in a single batch process. The improvement of the electrocatalytic activity is currently under ongoing research to determine the role of the iron oxide, as well as the effective presence of atomic iron catalytic sites. Also, improvement of the iron functionalization step itself is still studied. Iron functionalization of GNFs in hotter areas of the thermal plasma reactor is considered to increase the chances of a direct contact between the GNFs and iron vapour. The addition of a higher amount of nitrogen functionalities would be another way to improve the electrocatalytic activity of the catalysts.

Acknowledgements

We acknowledge Pierre Pascone for help with Raman measurements and insightful discussions. We also acknowledge the funding contributions from the *McGill Engineering Doctoral Award* (MEDA), the *Fonds de Recherche Nature et Technologie du Quebec* (FRNTQ) and from *Natural Science and Engineering Research Council* (NSERC) of Canada.

References

[1] J.-H. Wee, Renew. Sustain. Energy Rev. 11 (2007) 1720–1738, http://dx.doi.org/10.1016/j.rser.2006.01.005.
[2] V. Tripkovic, E. Skulason, S. Siahrostami, J.K. Norskov, J. Rossmeisl, Electrochim. Acta 55 (2010) 7975–7981, http://dx.doi.org/10.1016/j.electacta.2010.02.056.
[3] L. Zhang, J. Zhang, D.P. Wilkinson, H. Wang, J. Power Sources 156 (2006) 171–182, http://dx.doi.org/10.1016/j.jpowsour.2005.05.069.
[4] K. Niu, B. Yang, J. Cui, J. Jin, X. Fu, Q. Zhao, et al., J. Power Sources 243 (2013) 65–71, http://dx.doi.org/10.1016/j.jpowsour.2013.06.007.
[5] H.R. Byon, J. Suntivich, Y. Shao-Horn, Chem. Mater. 23 (2011) 3421–3428, http://dx.doi.org/10.1021/cm2000649.
[6] X. Zhang, W. Ouyang, D. Zeng, Y. Zhan, F. Xie, W. Zhang, et al., Catal. Today (2015), http://dx.doi.org/10.1016/j.cattod.2015.07.009.
[7] C.W.B. Bezerra, L. Zhang, K. Lee, H. Liu, A.L.B. Marques, E.P. Marques, et al., Electrochim. Acta 53 (2008) 4937–4951, http://dx.doi.org/10.1016/j.electacta.2008.02.012.

[8] Z. Wang, C.J. Liu, Nano Energy 11 (2015) 277–293, http://dx.doi.org/10.1016/j.nanoen.2014.10.022.
[9] R. Jasinski, Nature 201 (1964) 1212–1213, http://dx.doi.org/10.1038/2011212a0.
[10] U.I. Kramm, J. Herranz, N. Larouche, T.M. Arruda, M. Lefèvre, F. Jaouen, et al., Phys. Chem. Chem. Phys. 14 (2012) 11673–11688, http://dx.doi.org/10.1039/c2cp41957b.
[11] Z. Wu, S. Yang, Y. Sun, K. Parvez, X. Feng, K. Müllen, J. Am. Chem. Soc. 134 (2012) 9082–9085, http://dx.doi.org/10.1021/ja3030565.
[12] J.H. Yang, Y. Gao, W. Zhang, P. Tang, J. Tan, A.H. Lu, et al., J. Phys. Chem. C 117 (2013) 3785–3788, http://dx.doi.org/10.1021/jp311051g.
[13] L. Cui, G. Lv, Z. Dou, X. He, Electrochim. Acta 106 (2013) 272–278, http://dx.doi.org/10.1016/j.electacta.2013.05.077.
[14] C. Zhang, R. Hao, H. Yin, F. Liu, Y. Hou, Nanoscale (2012) 7326–7329, http://dx.doi.org/10.1039/c2nr32612d.
[15] P.-A. Pascone, D. Berk, J.-L. Meunier, Catal. Today 211 (2013) 162–167, http://dx.doi.org/10.1016/j.cattod.2013.03.026.
[16] S. Abdolhosseinzadeh, H. Asgharzadeh, H. Seop Kim, Sci. Rep. 5 (2015) 10160, http://dx.doi.org/10.1038/srep10160.
[17] E. Proietti, F. Jaouen, M. Lefevre, N. Larouche, J. Tian, J. Herranz, et al., Nat. Commun. 2 (2011) 1–6, http://dx.doi.org/10.1038/ncomms1427.
[18] P.-A. Pascone, J. de Campos, J.-L. Meunier, D. Berk, Appl. Catal. B Environ. 193 (2016) 9–15, http://dx.doi.org/10.1016/j.apcatb.2016.04.002.
[19] R. Pristavita, N.Y. Mendoza-Gonzalez, J.L. Meunier, D. Berk, Plasma Chem. Plasma Process. 30 (2010) 267–279, http://dx.doi.org/10.1007/s11090-010-9218-7.
[20] R. Pristavita, J.L. Meunier, D. Berk, Plasma Chem. Plasma Process. 31 (2011) 393–403, http://dx.doi.org/10.1007/s11090-011-9289-0.
[21] D.M. Binny, J.L. Meunier, D. Berk, Proc. IEEE Conf. Nanotechnol. (2012) 5–10, http://dx.doi.org/10.1109/NANO.2012.6322208.
[22] J.L. Meunier, N.Y. Mendoza-Gonzalez, R. Pristavita, D. Binny, D. Berk, Plasma Chem. Plasma Process. (2014) 505–521, http://dx.doi.org/10.1007/s11090-014-9524-6.
[23] U. Legrand, N.-Y. Mendoza Gonzalez, P. Pascone, J.-L. Meunier, D. Berk, Carbon N. Y. 102 (2016) 216–223, http://dx.doi.org/10.1016/j.carbon.2016.02.043.
[24] K. Shinozaki, J.W. Zack, R.M. Richards, B.S. Pivovar, S.S. Kocha, J. Electrochem. Soc. 162 (2015) F1144–F1158, http://dx.doi.org/10.1149/2.1071509jes.
[25] S.S. Kocha, Y. Garsany, D. Myers, Testing Oxygen Reduction Reaction Activity with the Rotating Disc Electrode Technique, DOE Webinar, 2013 http://energy.gov/eere/fuelcells/downloads/testing-oxygen-reduction-reaction-activity-rotating-disc-electrode.
[26] N. Ohno, M. Yoshimi, M. Tokitani, S. Takamura, K. Tokunaga, N. Yoshida, J. Nucl. Mater. 390–391 (2009) 61–64, http://dx.doi.org/10.1016/j.jnucmat.2009.01.051.
[27] J. Lu, X. Jiao, D. Chen, W. Li, Nanoplates (2009) 4012–4017.
[28] N. Larouche, B.L. Stansfield, Carbon N. Y. 48 (2010) 620–629, http://dx.doi.org/10.1016/j.carbon.2009.10.002.
[29] Q. Wei, X. Tong, G. Zhang, J. Qiao, Q. Gong, S. Sun, Catalysts 5 (2015) 1574–1602, http://dx.doi.org/10.3390/catal5031574.
[30] T. Yamashita, P. Hayes, Appl. Surf. Sci. 254 (2008) 2441–2449, http://dx.doi.org/10.1016/j.apsusc.2007.09.063.
[31] S. Pylypenko, S. Mukherjee, T.S. Olson, P. Atanassov, Electrochim. Acta 53 (2008) 7875–7883, http://dx.doi.org/10.1016/j.electacta.2008.05.047.
[32] C. Song, J. Zhang, PEM Fuel Cell Electrocatal. Catal. Layers (2008) 89–134, http://dx.doi.org/10.1007/978-1-84800-936-3_2.
[33] W. Zhou, L. Ge, Z.G. Chen, F. Liang, H.Y. Xu, J. Motuzas, et al., Chem. Mater. 23 (2011) 4193–4198, http://dx.doi.org/10.1021/cm201439d.
[34] R. Subramanian, Aerosol Air Qual. Res. 9 (2009) 172–186.